Light scattering by hexagonal ice crystals: solutions by a ray-by-ray integration algorithm

Ping Yang and K. N. Liou

Center for Atmospheric and Remote Sounding Studies/Department of Meteorology, University of Utah, Salt Lake City, Utah 84112

Received August 19, 1996; revised manuscript received January 21, 1997; accepted February 24, 1997

A ray-by-ray integration (RBRI) method has been developed for the solution of light scattering by nonspherical dielectric particles. The principles of geometric optics are applied to solve the internal electric field within the scattering particles (near field) with the inclusion of complete phase and polarization configurations. The scattered field at the radiation zone (far field) and the extinction and absorption cross sections are obtained by integrating the near field along the propagation paths of geometric rays inside the scatterers by using a number of rigorous electromagnetic integral equations. In the computations of extinction cross section and single-scattering albedo, we demonstrate that the well-known anomalous diffraction approximation is a special case of the RBRI method when the scatterers are optically tenuous. The RBRI method is employed to compute the single-scattering properties of hexagonal ice crystals at visible and near-infrared wavelengths. Based on the reference results computed by the finite-difference time domain (FDTD) technique, we show that the RBRI method is more accurate than the conventional geometric ray-tracing technique and the anomalous diffraction approximation. The extinction efficiency and the single-scattering albedo computed by the RBRI method converge to the reference results when the size parameters along the ice crystal maximum dimension are larger than approximately 15. Substantial differences in terms of relative errors, in comparison with the FDTD solutions, are still noted in the phase function and polarization patterns computed by the RBRI method for size parameters of the order of 10. © 1997 Optical Society of America [S0740-3232(97)01009-0]

1. INTRODUCTION

The importance of globally distributed cirrus clouds has been widely recognized in the fields of remote sensing, radiative transfer, the energy budget in the Earth–Atmosphere system, and climate modeling.[1,2] As discussed by Liou and Takano,[3] an understanding of the radiative characteristics of cirrus clouds must begin with a proper understanding of the single-scattering properties of nonspherical ice crystals. From *in situ* observations based on airborne optical probes and a balloon-borne replicator, the shapes of ice crystals are predominately solid and hollow hexagonal columns, plates, bullet rosettes, and aggregates.[4–8] Other irregular shapes, such as dendrites and capped columns, have also been observed.[9] A couple of recent investigations[10,11] have shown that using area- or volume-equivalent ice spheres to approximate nonspherical ice crystals for the computations of scattering, absorption, and polarization properties is inadequate and often misleading. Because our physical understanding of the scattering and absorption behavior of naturally occurring ice crystals is still limited, this specific scientific issue is currently an area of substantial research interest.

The exact solution of a vector wave equation with the boundary condition for a hexagonal ice particle appears to be not possible, because proper coordinate systems for the separation of the Helmholtz equation cannot be defined and imposed. Although several accurate numerical methods, which have been summarized by Liou and Takano[3] and Yang and Liou[12] and in the references cited therein, have been developed for the solution of light scattering by nonspherical particles, they are applicable only to small size parameters (<10) in practice because of numerical instability and enormous demands on computer resources, particularly when the orientations and the size distributions of ice crystals are required in the calculations.

In the past two decades, investigations of the scattering and absorption properties of ice crystals have been carried out extensively on the basis of geometric optics in terms of the ray-tracing technique (hereafter referred to as the conventional geometric-optics method, or GOM1).[13–15] As discussed by the present authors,[12] GOM1 suffers a number of disadvantages, particularly with the assumption of a constant extinction efficiency of 2, which is equally contributed by diffraction and Fresnelian reflections and refractions regardless of particle size parameters. However, the extinction efficiency determined from the fundamental electromagnetic theory is an oscillating function of size parameter, converging to 2 only at very large size parameters. For this reason GOM1 leads to significant errors in computing the extinction and scattering cross sections for small size parameters. Substantial errors in computing the phase matrix by GOM1 for small size parameters can also be produced by the assumption that the scattered energy in a specified direction can be obtained by summing the energy carried by the rays that emerge in a small element of solid angle around this direction. It has been estimated that GOM1 can be applied to size parameters larger than approximately 50 or 100, depending on whether the computations

0740-3232/97/0902278-12$10.00

are for the scattering cross section or the phase matrix, respectively.

In the present investigation, we have developed a novel geometric-optics method in an attempt to extend the applicable regime of GOM1 to moderate size parameters. In this method the principles of geometric optics are used to solve the internal electric field within a dielectric particle (near field), in which the complete phase and polarization patterns of the localized waves are accounted for. Subsequently, a ray-by-ray integration (RBRI) algorithm is developed on the basis of a number of rigorous electromagnetic relationships for computations of the scattered field at the radiation zone (far field), the extinction cross section, and the single-scattering albedo. In the computations of extinction and absorption cross sections, the RBRI method can be regarded as an extension of the well-known anomalous diffraction approximation (ADA), originally developed by van de Hulst,[16] for "optically soft" (refractive index close to 1) particles.

The present paper is organized as follows. In Section 2 the RBRI method is developed to solve the scattering properties of a dielectric particle. In this section we also demonstrate the equivalence of the RBRI and ADA methods in the computations of extinction and absorption cross sections in optically soft cases. Numerical results computed by the RBRI method in conjunction with the scattering of light by hexagonal ice crystals at visible and near-infrared wavelengths are presented in Section 3, in which it is also validated against the "exact" finite-difference time domain (FDTD) numerical technique. Finally, conclusions are given in Section 4.

2. NOVEL GEOMETRIC-OPTICS METHOD FOR LIGHT SCATTERING BY DIELECTRIC OBJECTS

A. Ray-by-Ray Integration Algorithm

Consider the scattering of light by a dielectric particle. The scattered field can be obtained on the basis of the fundamental electromagnetic theory if the electric field within the particle is known. The scattered field at far field, i.e., $kr \to \infty$, can be related to the internal field as follows[17]:

$$\mathbf{E}^s(\mathbf{r})|_{kr\to\infty} = \frac{k^2 \exp(ikr)}{4\pi r}(\epsilon - 1)\iiint_v \{\mathbf{E}(\mathbf{r}') - \hat{r}[\hat{r}\cdot\mathbf{E}(\mathbf{r}')]\}\exp(-ik\hat{r}\cdot\mathbf{r}')\mathrm{d}^3r', \quad (1)$$

where $\mathbf{E}$ is the internal electric field within the particle. $\mathbf{E}^s$ is the scattered far field, ϵ is the permittivity, k is the wave number of the electromagnetic wave in vacuum, and the domain of the integral, v, is the region inside the particle. Furthermore, according to the conservation principle of electromagnetic energy concerning the Poynting vector,[18] it can be proven that the extinction and absorption cross sections of the particle can be obtained, respectively, by the following equations:

$$\sigma_e = \mathrm{Im}\left[\frac{k}{|\mathbf{E}_0|^2}(\epsilon - 1)\iiint_v \mathbf{E}(\mathbf{r}')\cdot\mathbf{E}_0{}^*(\mathbf{r}')\mathrm{d}^3r'\right], \quad (2)$$

$$\sigma_a = \frac{k}{|\mathbf{E}_0|^2}\epsilon_i\iiint_v \mathbf{E}(\mathbf{r}')\cdot\mathbf{E}^*(\mathbf{r}')\mathrm{d}^3r', \quad (3)$$

where the asterisk denotes the complex conjugate, ϵ_i is the imaginary part of permittivity, and $\mathbf{E}_0$ is the electric field associated with the initial or incident wave. Equations (1)–(3) provide a framework to solve the scattering properties of nonspherical particles by various numerically accurate methods to obtain the near field involved in the integrands, such as the digitized Green's-function method[19] (which is closely related to the discrete dipole approximation)[20] and the FDTD technique.[12,21] These methods require formidable computational efforts for size parameters larger than approximately 10. To economize the computational requirement, researchers have developed, over many years, numerous approximate approaches to provide reasonable guesses for the internal field $\mathbf{E}(\mathbf{r}')$ in Eqs. (1)–(3), such as the Rayleigh–Gans theory[16,22] (also known as the first-order Born approximation in quantum mechanics), the technique of small-perturbation expansion,[23] and the Wentzel–Kramers–Brillouin approximation[24] (a close ally of the high-energy or eikonal approximation[25]). These approaches, however, do not account for the effect of the particle boundary, i.e., the reflection and the refraction at the particle surface. For this reason they are valid only for the scattering problems concerning optically tenuous or soft objects. To deal with an optically thick case for which the boundary effect cannot be neglected, we apply the RBRI technique to solve the internal field. Since geometric optics is an asymptotic form of the rigorous electromagnetic wave theory, the prerequisite for the present method is that the size parameter be sufficiently large so that the localization of geometric-optics rays does not lead to significant errors.

Under the geometric-optics approximation, the incident wave can be regarded as consisting of a bundle of localized waves or geometric rays each of which propagates along the rectilinear path determined by the Snell law, with deviation of propagation only on the particle surface. The amplitude of the electric field can be calculated by using the Fresnel formulas for the localized waves. As shown in Fig. 1(a), let the order of the internal localized waves within the particle be denoted by subscript index p (=1, 2, 3, …). It can be proven that the propagation directions of the localized waves may be specified by the following unit vectors:

$$\hat{e}_1 = N_r{}^{-1}\{\hat{e}_0 - (\hat{e}_0\cdot\hat{n}_1)\hat{n}_1 - [N_r{}^2 - 1 + (\hat{e}_0\cdot\hat{n}_1)^2]^{1/2}\hat{n}_1\}, \quad (4a)$$

$$\hat{e}_p = \hat{e}_{p-1} - 2(\hat{e}_{p-1}\cdot\hat{n}_p)\hat{n}_p, \qquad p = 2, 3, 4, \ldots, \quad (4b)$$

where N_r is the real part of an adjusted refractive index N that accounts for the inhomogeneous effect of refraction when the particle is absorptive,[12] $\hat{e}_0$ is the incidence direction, and $\hat{n}_p$ is the outward-pointing normal direction at the location of incidence point Q_p on the particle surface at which the Fresnelian reflection and refraction occur. The polarization configuration of the electric field associated with the localized waves can be determined with respect to the unit vectors that are perpendicular

and parallel to the incidence plane containing the incoming and outgoing rays. These unit vectors can be specified by

$$\hat{\beta}_p = (\hat{n}_p \times \hat{e}_p)[1 - (\hat{e}_p \cdot \hat{n}_p)^2]^{-1/2}, \qquad p = 1, 2, 3, \ldots, \tag{5a}$$

$$\hat{\alpha}_p = \hat{e}_p \times \hat{\beta}_p, \qquad p = 1, 2, 3, \ldots . \tag{5b}$$

When $(\hat{e}_p \cdot \hat{n}_p)^2 = 1$, the incidence plane cannot be specified uniquely for an incoming localized wave. In this case we choose $\hat{\beta}_p = \hat{\beta}_{p-1}$ (note that the incidence polarization configuration is determined by the unit vectors $\hat{\alpha}_0$ and $\hat{\beta}_0$). The induced electric field associated with the pth-order localized wave can be decomposed with respect to the unit vectors defined by Eqs. (5) as follows:

$$\mathbf{E}_p(\mathbf{r}) = \hat{\alpha}_p E_{p,\alpha}(\mathbf{r}) + \hat{\beta}_p E_{p,\beta}(\mathbf{r}). \tag{6}$$

Using the ray-tracing technique and accounting for the complete phase information for the localized waves, we can express the preceding internal field in the form

$$\begin{pmatrix} E_{p,\alpha}(\mathbf{r}) \\ E_{p,\beta}(\mathbf{r}) \end{pmatrix} = \begin{cases} \mathbf{U}_p \mathbf{A} \exp[i\,\delta_p(\mathbf{r})], & \mathbf{r} \in \text{ ray path} \\ 0, & \mathbf{r} \notin \text{ ray path} \end{cases} \tag{7a}$$

for $p = 1, 2, 3, \ldots$, where

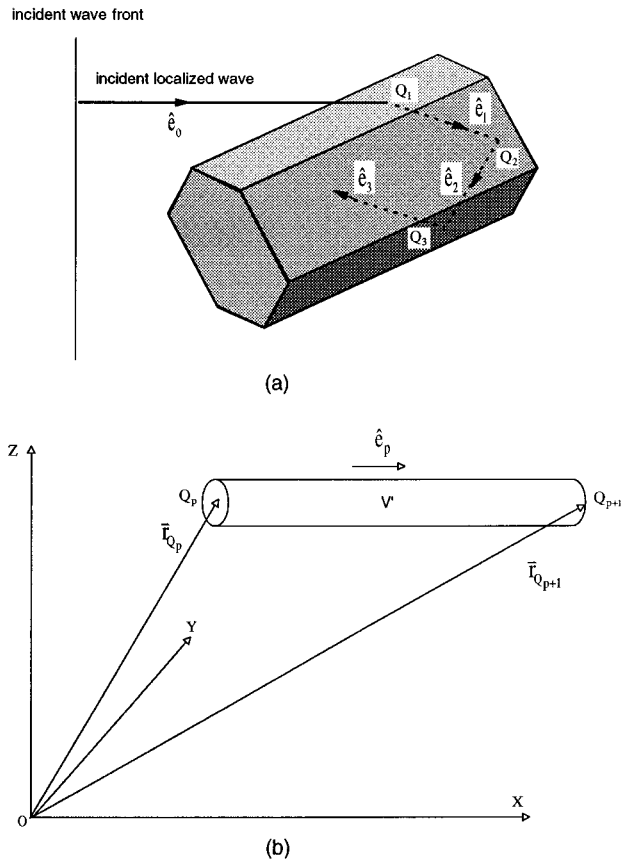

Fig. 1. (a) Geometry for the ray-by-ray integration (RBRI) algorithm for light scattering by a hexagonal ice crystal; (b) segment of the ray path within the ice crystal, in which a circular cross section has been assumed for the ray path.

$$\delta_p(\mathbf{r}) = k\left[\hat{e}_0 \cdot \mathbf{r}_{Q_1} + N\sum_{j=1}^{p-1} d_j + N\hat{e}_p \cdot (\mathbf{r} - \mathbf{r}_{Q_p})\right], \tag{7b}$$

$$d_j = |\mathbf{r}_{Q_{j+1}} - \mathbf{r}_{Q_j}|, \tag{7c}$$

$\mathbf{A}$ is the amplitude of the incident wave expressed in matrix form with the components projected in the directions specified by $\hat{\alpha}_0$ and $\hat{\beta}_0$, $\mathbf{U}_p$ is a 2×2 matrix that can be calculated by a set of recursive equations involving the Fresnelian reflection and refraction coefficients and two-dimensional rotational transformations for the coordinate systems specified by $\hat{\alpha}_{p-1}$ and $\hat{\beta}_{p-1}$ and by $\hat{\alpha}_p$ and $\hat{\beta}_p$, and $\mathbf{r}_{Q_p}$ is the position vector of point Q_p. After the internal electric fields associated with the localized waves are determined by Eqs. (6) and (7), the volume integrals in Eqs. (1)–(3) can be computed along the spatial path of each individual localized wave.

To determine the polarization configuration of the scattered waves, we let the unit vectors, which are parallel and perpendicular to the scattering plane, be given by $\hat{\eta}$ and $\hat{\xi}$, respectively. These two vectors are related to the scattering direction $\hat{r}$ by the following equation:

$$\hat{r} = \hat{\xi} \times \hat{\eta}. \tag{8}$$

Then the scattering field produced by the pth-order ray can be decomposed as follows:

$$\mathbf{E}_p^s(\mathbf{r}) = \hat{\eta} E_{p,\eta}^s(\mathbf{r}) + \hat{\xi} E_{p,\xi}^s(\mathbf{r}), \qquad p = 1, 2, 3, \ldots . \tag{9}$$

The preceding two components of the scattered field can be expressed by using the amplitude scattering matrix $\mathbf{S}_p(\hat{r})$ and the incident field in the form

$$\begin{pmatrix} E_{p,\eta}^s(\mathbf{r}) \\ E_{p,\xi}^s(\mathbf{r}) \end{pmatrix} = \frac{\exp(ikr)}{-ikr} \mathbf{S}_p(\hat{r}) \mathbf{A}_s, \tag{10}$$

where $\mathbf{A}_s$ is the incidence amplitude that is decomposed with respect to the scattering plane. On substitution of Eq. (7a) into Eq. (1), the amplitude scattering matrix contributed by the segment of the pth-order localized wave is given by

$$\mathbf{S}_p(\hat{r}) = \frac{ik^3(1 - \epsilon)}{4\pi} q_p(\hat{r}) \mathbf{K}_p \mathbf{U}_p \boldsymbol{\Gamma}, \tag{11a}$$

where

$$q_p(\hat{r}) = \iiint_{v'} \exp\{i[\delta_p(\mathbf{r}') - k\hat{r} \cdot \mathbf{r}']\} \mathrm{d}^3 r', \tag{11b}$$

$$\mathbf{K}_p = \begin{bmatrix} \hat{\eta} \cdot \hat{\alpha}_p & \hat{\eta} \cdot \hat{\beta}_p \\ \hat{\xi} \cdot \hat{\alpha}_p & \hat{\xi} \cdot \hat{\beta}_p \end{bmatrix}, \tag{11c}$$

and $\boldsymbol{\Gamma}$ is a two-dimensional rotational matrix that transforms $\mathbf{A}_s$ to $\mathbf{A}$, defined in Eq. (7a). The integral domain in Eq. (11b), v', is the spatial region occupied by the ray path, as shown in Fig. 1(b).

To make the preceding algorithm practical in numerical computation, the integral in Eq. (11b) must be solved analytically. This is very difficult in ray-tracing calculations because the geometric shape of the ray cross sections cannot be determined exactly with reasonable computational effort after an initial ray with a given cross-

section shape is refracted into the particle. For simplicity, circular cross sections are assumed for all the rays inside the particle. Based on the geometry shown in Fig. 1(b), a position vector inside the segment of ray path between two points Q_p and Q_{p+1} can be expressed as follows:

$$\mathbf{r}' = \mathbf{r}_{Q_p} + e\hat{e}_p + u\hat{u}_p + v\hat{v}_p, \qquad \mathbf{r}' \in v', \tag{12}$$

where $\hat{u}_p$ and $\hat{v}_p$ are two orthogonal unit vectors perpendicular to the unit vector $\hat{e}_p$. Thus, by substituting Eqs. (7b) and (12) into Eq. (11b), we obtain

$$\begin{aligned} q_p(\hat{r}) = \exp\left[ik\left(\hat{e}_0 \cdot \mathbf{r}_{Q_1} + N\sum_{j=1}^{p-1} d_j - \hat{r} \cdot \mathbf{r}_{Q_p}\right)\right] \\ \times \int_0^{d_p} \exp[ik(N - \hat{r} \cdot \hat{e}_p)e]\mathrm{d}e \\ \times \iint_{\substack{\text{ray cross}\\ \text{section}}} \exp[-ik\hat{r} \cdot (u\hat{u}_p + v\hat{v}_p)]\mathrm{d}u\,\mathrm{d}v. \end{aligned} \tag{13}$$

After some mathematical manipulations, we obtain the explicit expression

$$\begin{aligned} q_p(\hat{r}) = \Delta\tilde{\sigma}_p\{\exp[i\zeta_{p+1}(\hat{r})] \\ - \exp[i\zeta_p(\hat{r})]\}/[ik(N - \hat{r} \cdot \hat{e}_p)], \end{aligned} \tag{14a}$$

where

$$\zeta_p(\hat{r}) = k\left(\hat{e}_0 \cdot \mathbf{r}_{Q_1} + N\sum_{j=1}^{p-1} d_j - \hat{r} \cdot \mathbf{r}_{Q_p}\right) \tag{14b}$$

and the phase interference integrated over the ray cross section is given by

$$\begin{aligned} \Delta\tilde{\sigma}_p &= \iint_{\substack{\text{ray cross}\\ \text{section}}} \exp[-ik\hat{r} \cdot (u\hat{u}_p + v\hat{v}_p)]\mathrm{d}u\,\mathrm{d}v \\ &= \Delta\sigma_p 2J_1(\chi)/\chi, \end{aligned} \tag{14c}$$

in which $\Delta\sigma_p$ is the cross-section area of the pth-order ray and $J_1(\chi)$ is the first-order Bessel function of the argument χ, defined by

$$\chi = k(\Delta\sigma_p/\pi)^{1/2} \sin[\cos^{-1}(\hat{e}_p \cdot \hat{r})]. \tag{14d}$$

In Eq. (14c) the circular cross section is implied for the ray path. Based on various numerical tests, we find that the computed single-scattering properties are not sensitive to the dimension of the circular cross section if its radius is smaller than approximately $\lambda/2\pi$, where λ is the incidence wavelength. For this reason we have selected the radius of the ray cross section as $\lambda/2\pi$ in numerical computations. The total rays employed in the numerical computation are therefore of the order of k^2P/π, in which k is the incidence wave number and P is the projected area of the particle along the incidence direction. Furthermore, it should be pointed out that the effect of the shape of the ray-path cross section is not significant when it is small, because $\lim_{\Delta\sigma_p \to 0} \Delta\tilde{\sigma}_p = \Delta\sigma_p$ regardless of the shape of the ray cross section. By using Eq. (14a), we can express the scattering matrix in a form that is suitable for numerical computations as follows:

$$\begin{aligned} \mathbf{S}_p(\hat{r}) = \frac{k^2}{4\pi}\frac{\Delta\tilde{\sigma}_p}{N - \hat{r} \cdot \hat{e}_p}(1 - \epsilon)\mathbf{K}_p\mathbf{U}_p\mathbf{\Gamma} \\ \times \{\exp[i\zeta_{p+1}(\hat{r})] - \exp[i\zeta_p(\hat{r})]\}. \end{aligned} \tag{15}$$

The total scattering matrix is then given by summing the contributions from all the localized waves or geometric-optics rays as follows:

$$\mathbf{S}(\hat{r}) = \sum_{\gamma}\sum_{p=1}^{\infty} \mathbf{S}_p(\hat{r}), \tag{16}$$

where the summation over γ denotes the collection of the contributions of different initial or incident rays. After the amplitude scattering matrix is defined, the corresponding Stokes phase matrix can be determined and computed in a straightforward manner.

To understand the relationship between the preceding RBRI algorithm and GOM1, we rewrite Eq. (16) as follows:

$$\mathbf{S}(\hat{r}) = \sum_{\gamma}\sum_{p=1}^{\infty} \mathbf{S}_p(\hat{r}) = \sum_{p=1}^{\infty} \tilde{\mathbf{S}}_p(\hat{r}), \tag{17a}$$

where

$$\tilde{\mathbf{S}}_1(\hat{r}) = -\frac{k^2}{4\pi}(1 - \epsilon)\sum_{\gamma}\frac{\Delta\tilde{\sigma}_1}{N - \hat{r} \cdot \hat{e}_1}\mathbf{K}_1\mathbf{U}_1\mathbf{\Gamma}\exp(i\zeta_1), \tag{17b}$$

$$\begin{aligned} \tilde{\mathbf{S}}_p(\hat{r}) = \frac{k^2}{4\pi}(1 - \epsilon)\sum_{\gamma}\left(\frac{\Delta\tilde{\sigma}_{p-1}\mathbf{K}_{p-1}\mathbf{U}_{p-1}}{N - \hat{r} \cdot \hat{e}_{p-1}}\right. \\ \left. - \frac{\Delta\tilde{\sigma}_p\mathbf{K}_p\mathbf{U}_p}{N - \hat{r} \cdot \hat{e}_p}\right)\mathbf{\Gamma}\exp(i\zeta_p), \qquad p = 2, 3, 4, \ldots . \end{aligned} \tag{17c}$$

The phase configuration involved in Eq. (17b) corresponds to that associated with diffraction and external reflection, whereas ζ_p in Eq. (17c) is the phase of transmitted or refracted rays that undergo $p - 1$ internal reflections. Thus $\tilde{\mathbf{S}}_1$ stands for the contribution from diffraction and external reflection, whereas $\tilde{\mathbf{S}}_p (p \geq 2)$ denotes the contribution from the transmitted or refracted rays that undergo $p - 1$ times internal reflections. It should be pointed out that an analytic expression can be derived for $\tilde{\mathbf{S}}_1$ if the particle surface is locally planar, such as hexagonal plates and columns, as shown in Appendix A. In these cases the discrete summation over individual rays, denoted by index γ, can be replaced by a continuous integral evaluated for each individual planar surface of the particle. The analytic expression of $\tilde{\mathbf{S}}_1$ provides an efficient method in solving the phase matrix for strongly absorptive particles because the rays with $p > 1$ can be neglected.

Applying the same procedure of the preceding ray-by-ray calculation to Eq. (2), we obtain the extinction cross section in the form

$$\sigma_e = \frac{2\pi}{k^2}\mathrm{Re}[S_{11}(\hat{e}_0) + S_{22}(\hat{e}_0)], \tag{18}$$

where $S_{11}(\hat{e}_0)$ and $S_{22}(\hat{e}_0)$ are the diagonal elements of the amplitude scattering matrix in the forward direction. Clearly, the preceding equation is a recapture of the extinction or optical theorem under the geometric-optics approximation. Similarly, the absorption cross section is given by

$$\sigma_a = \frac{1}{2}\sum_{\gamma}\sum_{p=2}^{\infty}\Delta\sigma_p N_r \exp\left(-2kN_i\sum_{j=1}^{p-1} d_j\right) \times [1 - \exp(-2kN_i d_{p,\gamma})] \times (\mathbf{\Lambda}\mathbf{U}_p{}^{*}\mathbf{U}_p{}^{T}\mathbf{\Lambda}^T + \mathbf{\Pi}\mathbf{U}_p{}^{*}\mathbf{U}_p{}^{T}\mathbf{\Pi}^T), \tag{19a}$$

where

$$\mathbf{\Lambda} = (1 \quad 0), \qquad \mathbf{\Pi} = (0 \quad 1), \tag{19b}$$

and the superscript T denotes the transpose of the matrices. In light of the preceding discussion, it is evident that the inaccuracy of the RBRI method is mainly caused by calculating the internal electric field by means of geometric optics. Unlike the other approximate methods cited above, there is no restriction on the magnitude of the refractive index for the applicability of the RBRI method, which, however, is subject to the assumption of the localization principle. Since the internal field is solved by geometric-optics principles while the mapping of near field to far field is based on the electromagnetic theory, RBRI can be regarded as a geometric-optics/wave-theory hybrid method. In the computation of complete phase matrix elements for randomly oriented hexagonal ice crystals with size parameters of the order of 50, we find that an approximate 5-h CPU time is required on a Silicon-Graphics-Indigo-2 computer. The required CPU time, however, is less than 1 min if only cross sections are computed.

B. Equivalence of Ray-by-Ray Integration and Anomalous Diffraction Approximation in the Optically Tenuous Case

In this subsection we will show that RBRI is a generalized form of ADA in the computations of extinction and absorption cross sections and that the former reduces to ADA in the optically tenuous case. Pioneered by van de Hulst,[16] the ADA method has been widely used in scattering calculations because of its extreme simplicity in determining the extinction and absorption cross sections for nonspherical particles. Theoretically, two conditions are mandatory for the applicability of ADA: (1) size parameter $ka \gg 1$ and (2) $m - 1 \ll 1$, where m is the refractive index of the particle. The first condition allows the tracing of a ray through the scattering particle, while the second implies that the ray will not suffer significant deviation of its propagation when penetrating the particle surface. In addition, this second condition also implies that variation of the field amplitude associated with the transmitted rays caused by Fresnelian interactions can be neglected. Stephens[26] has proven that the performance of ADA for a size parameter much less than 1 is similar in accuracy to that for a large size parameter. In practice, the second condition has been found to be critical to the accuracy of the results computed from ADA. As estimated by Chylek and Klett[27] for spherical particle cases, the error produced by ADA is approximately 10% for a refractive index with a real part of 1.2. However, the error increases to 25% when the real part of the refractive index is 1.4.

We should not present the details of the ADA method in this paper because they can be found elsewhere.[16,27] Conceptually, the variation of field amplitude and the deviation of ray propagation are neglected in this approximation, but the phase delay suffered by the ray inside the particle is accounted for. According to these physical simplifications, the extinction cross section can be obtained on the basis of Huygens's principle as follows[16]:

$$\sigma_e = 2\iint_P [1 - \exp(-\tau)\cos\rho]\mathrm{d}^2p, \tag{20a}$$

$$\tau = kdm_i, \qquad \rho = kd(m_r - 1), \tag{20b}$$

where the integral domain P is the particle projection or shadow on a screen perpendicular to the incidence direction, m_r and m_i are the real and imaginary parts of the refractive index, and d is the length of the ray path inside the particle. The parameter ρ specifies the phase delay of the ray inside the particle, while τ determines the damping of the wave that is due to the particle absorption. It should be noted that both ρ and τ are functions of the coordinate values of the points inside the particle shadow. In ADA the absorption cross section of the particle is simply the summation of the absorption of individual rays within the particle such that

$$\sigma_a = \iint_P [1 - \exp(-2\tau)]\mathrm{d}^2p. \tag{21}$$

To prove that ADA is a special case of RBRI, we note that the scattered field computed by the latter method in an optically tenuous case is essentially from the first-order internal rays. Moreover, since the deviation of ray propagation can be neglected under the condition $m \sim 1$, the following approximations are valid:

$$\hat{e}_1 \approx \hat{e}_0, \tag{22a}$$

$$\mathbf{K}_1\mathbf{U}_1\mathbf{\Gamma} \approx \begin{bmatrix} 1 & 0 \\ 0 & 1 \end{bmatrix}. \tag{22b}$$

According to Eq. (14a) and relation (22a), we have in the forward-scattering direction the following expression:

$$\exp[i\zeta_2(\hat{e}_0)] - \exp[i\zeta_1(\hat{e}_0)] \approx \exp[ikd_1(N - 1)] - 1, \tag{23}$$

where d_1 is the path length of the first-order internal rays. Thus, from Eqs. (15), (16), and (18) and relations (22a) and (23), the extinction cross section is given by

$$\sigma_e = \mathrm{Re}\left(-\sum_{\gamma}\frac{\Delta\tilde{\sigma}_1(1 - \epsilon)}{N - 1}\{\exp[ikd_1(N - 1)] - 1\}\right). \tag{24}$$

Furthermore, when $m \sim 1$, we have the following approximation:

$$\frac{1 - \epsilon}{N - 1} = \frac{(1 - m)(1 + m)}{N - 1} \approx -(1 + m) \approx -2. \tag{25}$$

Under condition (22a) the parameter χ defined in Eq. (14d) is zero in the forward direction. It follows that

$$\Delta\tilde{\sigma}_1 = \Delta\sigma_1 \lim_{\chi\to 0} [2J_1(\chi)/\chi] = \Delta\sigma_1. \tag{26}$$

Although $\Delta\sigma_1$, by definition, is the ray cross section inside the particle, it is the same as that outside the particle in the optically soft case because the ray direction remains unchanged, as evident from Eq. (26). Thus Eq. (24) reduces to

$$\sigma_e = 2\sum_{\gamma} \Delta\sigma_1\{1 - \cos[kd_1(N_r - 1)]\exp(-kd_1N_i)\}. \tag{27}$$

Similarly, we can prove that Eq. (19a) reduces to

$$\sigma_a = \sum_{\gamma} \Delta\sigma_1[1 - \exp(-2kN_id_1)]. \tag{28}$$

Equations (27) and (28) are related to the adjusted refractive index N, which reduces to m under condition (22a). Thus RBRI is equivalent to ADA in the optically tenuous case, except that the discrete summation rather than the continuous integration is used in the RBRI formulation. This, however, makes no difference in numerical computations.

From the preceding discussion, it is clear that the ADA method is a special form of the RBRI method after a number of simplifications are made for the optically soft condition. In the optically thick case, i.e., when the condition $m - 1 \ll 1$ is not satisfied, the preceding simplifications are not valid, and ADA will produce considerable errors. At visible and near-infrared wavelengths, the refractive index of ice deviates from 1 by approximately 0.3–0.65. In these cases the deviation of ray propagation, the surface reflection and refraction, and the higher-order internal rays must be accounted for properly to obtain reliable scattering properties of ice crystals.

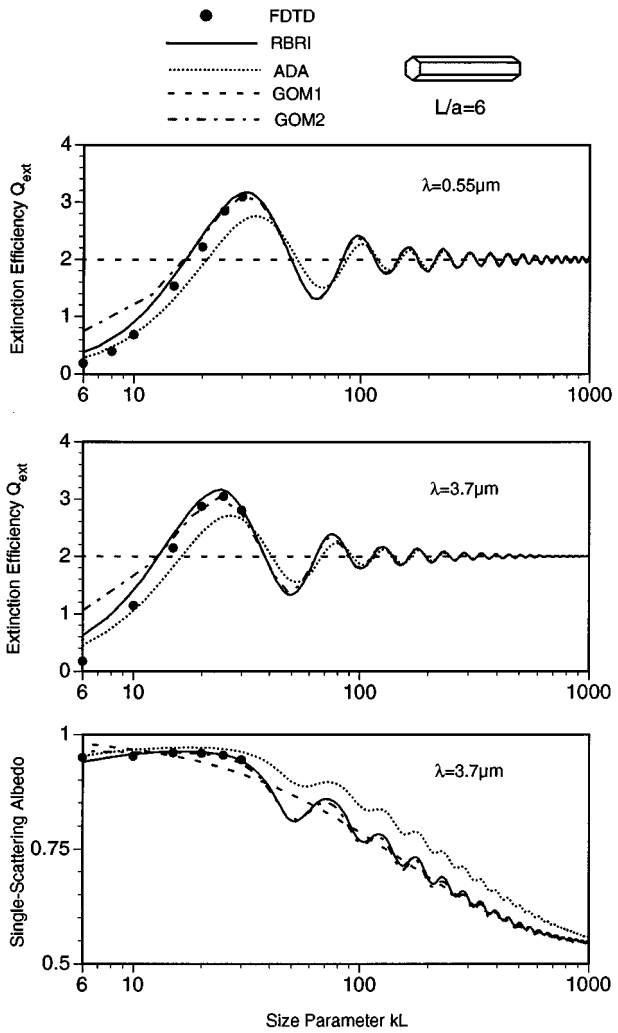

Fig. 2. Comparisons of the extinction efficiency and the single-scattering albedo computed by FDTD, RBRI, ADA, GOM2, and GOM1 at the 0.55-μm and 3.7-μm wavelengths.

3. NUMERICAL RESULTS AND DISCUSSION

In this section we present the scattering phase function, the extinction efficiency, and the single-scattering albedo for hexagonal ice crystals at the 0.55-μm and 3.7-μm wavelengths computed from the RBRI method. The complex refractive indices of ice at these two wavelengths are $1.311 + i3.11 \times 10^{-9}$ and $1.4005 + i7.1967 \times 10^{-3}$, respectively. Since this investigation emphasizes the scattering by small ice crystals, which generally do not have preferred orientations in the atmosphere on account of a small Reynolds number, ice crystals are assumed to be randomly oriented in the scattering calculations. The resolution of particle orientations employed in the present numerical computations is the same as that in our previous study.[21] Numerical computations are also carried out by using GOM1, GOM2, ADA, and FDTD. In the GOM2 approach developed by the present authors,[12,28] the geometric ray-tracing technique is applied to solve the tangential components of the electric and magnetic fields on a surface that encloses the scatterer. Subsequently, the tangential components of the electromagnetic field are used to determine the equivalent electric and magnetic currents that are then employed to compute the scattered far field on the basis of the electromagnetic equivalence theorem.[29] The FDTD technique has been applied by the present authors to the scattering of light by nonspherical ice crystals.[12,21] We have verified this technique by comparisons with exact solutions derived for the canonical problems involving long cylinders and spheres. Because the FDTD method has been found to give an excellent performance in the canonical problems, we have used the results computed from this method for hexagonal ice crystals as a reference in the following discussion.

Figure 2 shows the extinction efficiency and the single-scattering albedo computed by RBRI, GOM1, GOM2, ADA, and FDTD for hexagonal columns with an aspect ratio $L/a = 6$ for various size parameters. The computations by FDTD are limited to $kL \leqslant 30$ because of the limitation in computer resources. In Fig. 2 the size parameters are expressed in terms of the ice crystal maximum dimension. We note that the results computed by GOM2 and RBRI are very close when the size parameter kL is larger than approximately 15. The agreement of the two is due to the fact that knowing the field every-

where inside the particle or everywhere on the particle surface is equivalent in electrodynamics. However, substantial errors are produced by GOM2 for $kL < 15$ because of the localization of rays in the geometric-optics approximation and the assumption of a sharp division of illuminated and shadowed sides in this method. The transition of light intensity from the illuminated side to the shadowed side should be continuous because of the existence of surface waves,[12] which are particularly important for small size parameters.

For the extinction efficiency, a constant of 2 determined from GOM1 is not sufficiently accurate, particularly when the size parameter is small. Convergence of the extinction efficiency results obtained by GOM2, RBRI, and ADA to 2 is noted when the size parameter along the ice crystal minimum dimension is larger than approximately 50 (i.e., $kL = 300$). The extinction efficiencies computed by GOM2, RBRI, and ADA display fluctuations, with the last method showing the largest deviations from the FDTD results. This is because the optically tenuous condition required by ADA is not strictly applicable to the refractive indices at these two wavelengths. It is seen that the GOM2 and RBRI results essentially converge to the FDTD results when $kL > 15$. For size parameters $kL < 10$, large errors in the extinction efficiency computed by RBRI (or GOM2) are evident because of small ice crystal cross sections ($ka < 1.7$), in which the localization of geometric rays on the incidence wave front cannot be physically applied. We further note that the GOM2 and RBRI results deviate more than the ADA results when $kL < 10$. The reason is that higher-order rays are accounted for in RBRI (or GOM2); consequently, the errors produced by the localization approximation are more significant in these methods than in ADA.

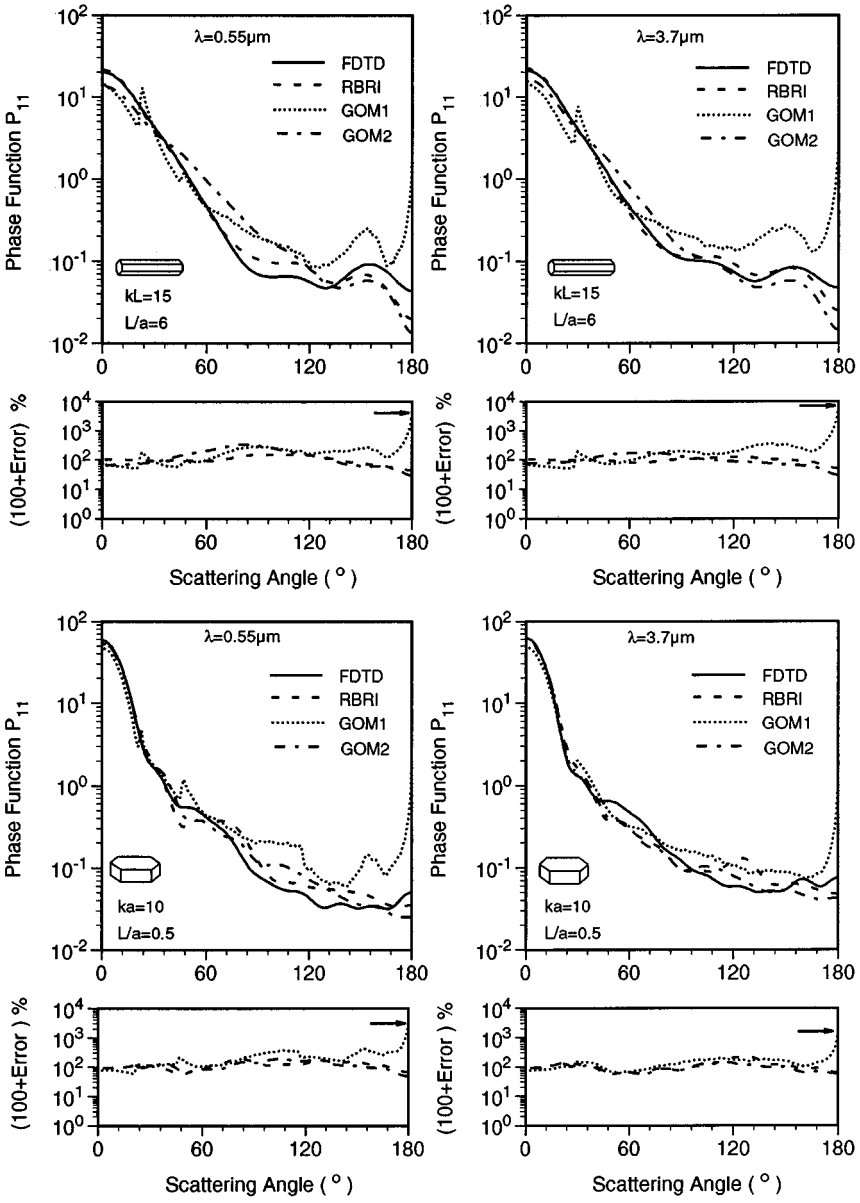

Fig. 3. Phase functions computed by FDTD, RBRI, GOM2, and GOM1 for hexagonal columns and plates. Also shown are the relative errors of the RBRI and GOM1 results in comparison with the reference results computed by FDTD. 100% has been added to the error values to avoid negative values in the logarithmic display.

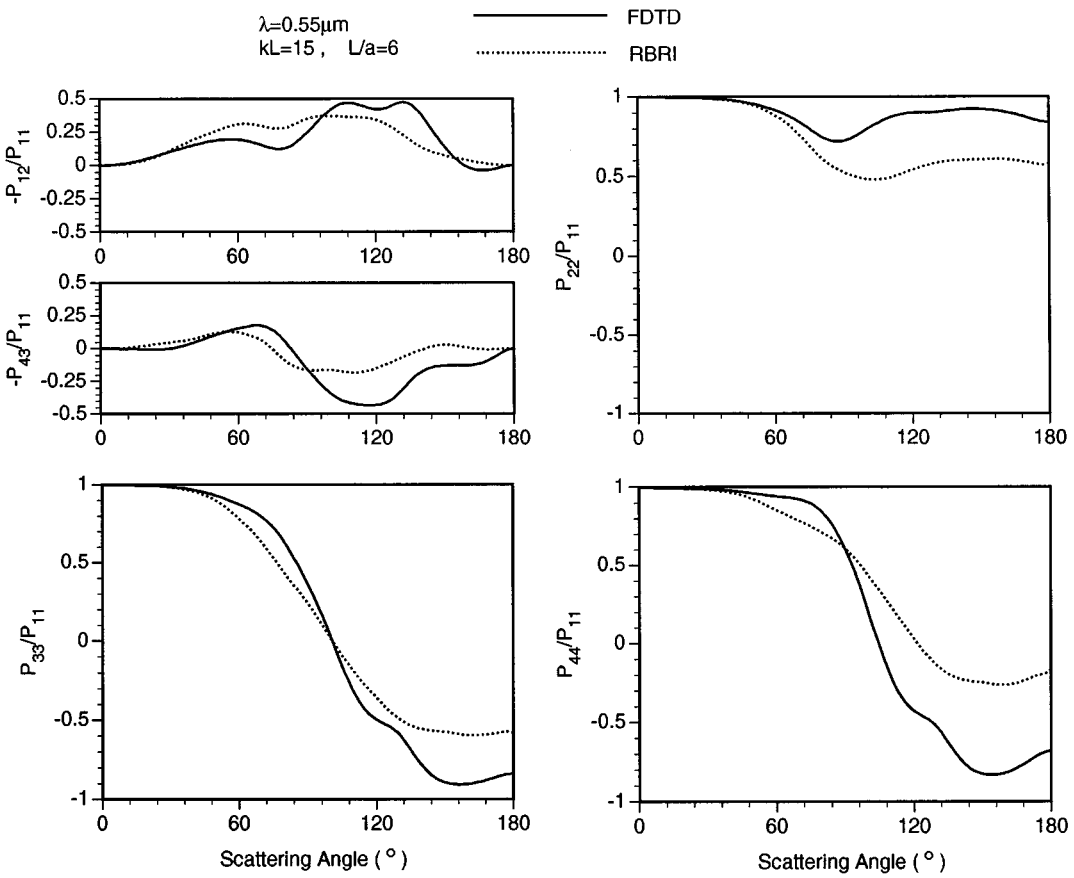

Fig. 4. Comparisons of the phase matrix elements computed by FDTD and RBRI for hexagonal columns.

For the single-scattering albedo at the 3.7-μm wavelength, substantial differences are found in the comparison of ADA, GOM2, and RBRI results. This is because only the first-order transmitted rays are accounted for in ADA, so that absorption of the scatterer is underestimated. Since the deviation of ray propagation is neglected in ADA, the lengths of ray paths computed by this method inside the particle are shorter than those computed by RBRI. It should be noted that the largest differences between the single-scattering albedo computed by ADA and RBRI occur in the region $kL = 35-400$. For smaller size parameters, particle absorption is relatively insignificant, so that the ADA and RBRI results are similar. For size parameter $kL > 400$, the rays refracted into the particle are essentially absorbed as a result of very long ray paths, leading to absorption saturation. For this reason the single-scattering albedos obtained by ADA and RBRI tend to converge. We find that the results computed by GOM1 are almost the mean values of the RBRI results if the fluctuation maxima and minima in the latter are smoothed out.

Presented in Fig. 3 are the scattering phase functions computed by FDTD, RBRI, GOM2, and GOM1 for hexagonal columns ($L/a = 6$) and plates ($L/a = 0.5$) at the wavelengths 0.55 μm and 3.7 μm. The relative errors of the results obtained by RBRI and GOM1 with respect to the FDTD solutions are also presented in the diagram, which are defined as

$$[P_{11}(\text{RBRI/GOM1}) - P_{11}(\text{FDTD})]/P_{11}(\text{FDTD}).$$

To display the relative errors on a logarithmic scale, we have added 100% to the error values so that negative values can be avoided. For columns, excellent agreement is noted between the FDTD and RBRI results in the scattering angle region 0°–60° at the visible wavelength. Better comparisons between the two are seen in the 3.7-μm-wavelength case. The RBRI method underestimates the backscattering in comparison with the "exact" FDTD solution. The GOM1 results show peaks at the 22° and 46° scattering angles for the 0.55-μm wavelength, a peak at the 29° scattering angle for the 3.7-μm wavelength, and maxima at the 154° scattering angle for both wavelengths. These features are not present in the FDTD and RBRI/GOM2 results. The overall angular scattering patterns computed by RBRI and GOM2 are similar, although the errors produced by GOM2 are larger because of the assumption of the abrupt transition of light intensity from the illuminated side to the shadowed side on the particle surface. These errors are more pronounced in the column case because of the small cross section involved. The relative errors for GOM1 in backscattering are 3917.7% and 6561.2% at the 0.55-μm and 3.7-μm wavelengths, respectively, while for GOM2 they are −69.7% and −69.9%, respectively. In the RBRI case, errors are −54.8% and −47.9%, respectively. For the plate case, GOM1 produces significant errors in the scattering angle region 90°–180° and the region near the 46° halo peak at the 0.55-μm wavelength. Pronounced errors are also found in backscattering at 3.7 μm. In back-

scattering the relative errors are 3166.0% and 1562.4% for GOM1, −50.4% and −43.0% for GOM2, and −30.8% and −36.3% for RBRI at the 0.55-μm and 3.7-μm wavelengths, respectively.

Figure 4 shows a comparison of the nonzero elements of the phase matrix computed by RBRI and FDTD for randomly oriented columns with $kL = 15$ and $L/a = 6$. Agreement is seen in the scattering angle region 0°–30°. Although overall patterns are similar, errors for RBRI are found for $-P_{12}/P_{11}$ and $-P_{43}/P_{11}$ in side-scattering directions and for P_{22}/P_{11}, P_{33}/P_{11}, and P_{44}/P_{11} in side-scattering and backscattering directions. The polarization configuration of the scattered field is clearly sensitive to the errors produced by the approximation of the internal field within the particle by means of the geometric-optics approach.

Figure 5 shows the phase functions computed by RBRI, GOM2, and GOM1 for hexagonal columns and plates that have the same aspect ratios as those in Fig. 3 but with larger size parameters. Computations by FDTD are not carried out for these size parameters because of the limitation in computer resources. Deviations in terms of the percentage of the results computed by RBRI (or GOM2) from those computed by GOM1 are defined as

$$[P_{11}(\text{GOM1}) - P_{11}(\text{RBRI/GOM2})]/P_{11}(\text{GOM1}).$$

200% has been added to these deviations in order that negative values can be avoided for a logarithmic display. Halo peaks and strong backscattering are not generated in the RBRI results. The percentage differences in backscattering between the RBRI and GOM1 results are 92.9% and 88.5% for the column case at 0.55 μm and 3.7

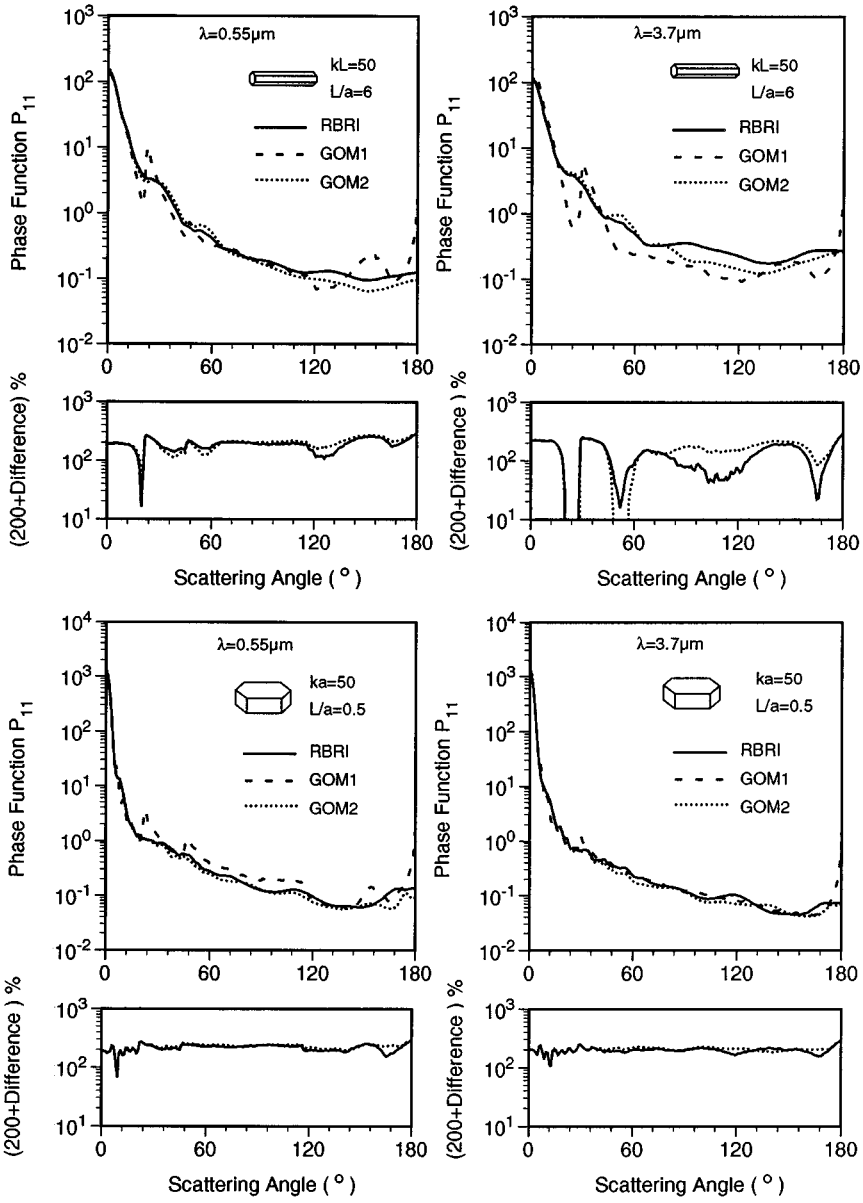

Fig. 5. Comparisons of the phase function computed by RBRI (GOM2) and GOM1 for size parameters $kL = 50$ ($L/a = 6$) and $ka = 50$ ($L/a = 0.5$). Also shown are the differences between RBRI (GOM2) and GOM1. 200% has been added to the error values so that negative values can be avoided in the logarithmic display.

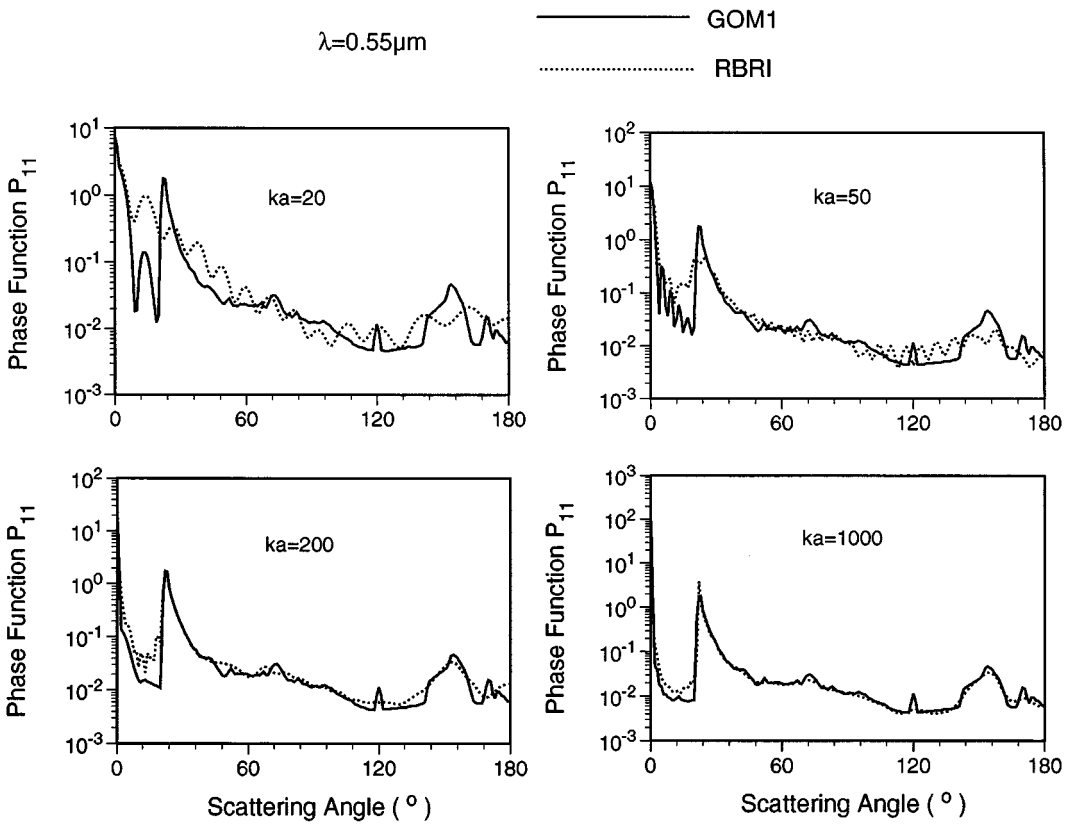

Fig. 6. Comparisons of the phase function computed by GOM1 and RBRI for infinitely long hexagonal cylinders randomly oriented around their axes with normal incidence.

μm, respectively. They are 91.9% and 92.8% for the plate case at the two wavelengths, respectively. Differences between GOM2 and GOM1 results are similar. The three approximate methods agree better in the plate case because the cross section is still quite small for columns ($ka \sim 8.33$). Note that for the plate case, both the length and width dimensions are much larger ($ka = 25$ and $kL = 50$).

The RBRI method requires enormous computer time for the computation of the phase function for randomly oriented ice crystals with size parameters of the order of 1000. To show the convergence of the RBRI approach to the conventional GOM1 technique, we consider infinitely long hexagonal cylinders randomly rotated around their axes with normal incidence. Computations of the phase function are confined to a plane perpendicular to the cylindrical axes. Phase function results computed for size parameters $ka = 20$, 50, 200, and 1000 are shown in Fig. 6. For $ka = 20$ the diffraction contribution cannot be distinguished from the contribution from Fresnelian reflection and refraction in RBRI, producing fluctuating patterns associated with phase interferences. The forward-scattering peak computed by GOM1 is approximately a factor of 2 larger than that computed by RBRI. For $ka = 50$ the discrepancy of the two methods is confined to the scattering angle region 0°–20°. Also, RBRI shows a broader scattering maximum at 22° rather than a sharp peak and does not produce peaks at the 154° and 120° scattering angles. The two methods converge when $ka = 1000$.

4. CONCLUSIONS

We have developed a novel ray-by-ray integration algorithm for light scattering by nonspherical ice crystals, referred to as RBRI. This approach is a combination of the geometric-optics approximation and the rigorous electromagnetic wave theory. The internal electric field within the particle is obtained by the localized waves and evaluated by using the Fresnel formulas. The internal field is then transformed to the far field by means of the RBRI technique. In the computation of extinction and absorption cross sections, we prove that the RBRI method is a generalized extension of the well-known anomalous diffraction approximation applicable to optically tenuous particles.

Numerical computations for the light scattering by hexagonal ice crystals show that the RBRI results converge to the "exact" finite-difference time domain solutions for the computation of the extinction cross section and the single-scattering albedo for hexagonal ice crystals with size parameters of the order of 15. However, differences in the phase matrix elements are shown in the side-scattering and backscattering directions for $ka = 15$. We also show that the results computed from the RBRI and GOM2 approaches are similar with respect to the cross sections and the phase function. RBRI requires much more computer time in the computation of the phase matrix than does GOM2. However, the former is more efficient in the computation of the extinction and absorption cross sections because analytic equations can be

derived. In terms of the phase function, RBRI and GOM1 converge when the size parameter is larger than approximately 200. Finally, it is concluded that RBRI is an efficient method for the computation of extinction efficiency and single-scattering albedo for nonspherical ice crystals covering all applicable solar and thermal infrared wavelengths with acceptable accuracy.

APPENDIX A: ANALYTIC EXPRESSION FOR THE SCATTERING MATRIX IN A STRONGLY ABSORPTIVE CASE

When strong absorption is involved, the scattering matrix determined by Eq. (17a) reduces to

$$\mathbf{S}(\hat{r}) \approx \tilde{\mathbf{S}}_1(\hat{r}) = -\frac{k^2}{4\pi}(1-\epsilon)\sum_{\gamma}\frac{\Delta\tilde{\sigma}_1}{N-\hat{r}\cdot\hat{e}_1} \times \mathbf{K}_1\mathbf{U}_1\mathbf{\Gamma}\exp(i\zeta_1). \quad \text{(A1)}$$

For a hexagonal ice crystal with a locally planar surface, an analytic expression can be obtained for $\tilde{\mathbf{S}}_1(\hat{r})$ to economize numerical computations. Since the factor $\mathbf{K}_1\mathbf{U}_1\mathbf{\Gamma}/(N-\hat{r}\cdot\hat{e}_1)$ is the same for all the first-order refracted rays associated with a given crystal planar surface, summation over the index γ for various incident rays can be replaced by a continuous integration as follows:

$$\tilde{\mathbf{S}}_1(\hat{r}) = -\frac{k^2}{4\pi}(1-\epsilon)\sum_j\left(\frac{\mathbf{K}_1\mathbf{U}_1\mathbf{\Gamma}}{N-\hat{r}\cdot\hat{e}_1}\right)_j f_j D_j, \quad \text{(A2a)}$$

$$f_j = [1-(\hat{e}_1\cdot\hat{n}_1)^2]_j^{1/2}, \quad \text{(A2b)}$$

$$D_j = \iint_{\#j\ \text{face}} \exp[ik(\hat{e}_0-\hat{r})\cdot\mathbf{r}']\mathrm{d}^2r', \quad \text{(A2c)}$$

where the subscript index j indicates different illuminated planar surfaces. For hexagonal columns and plates, the maximum number of illuminated planar surfaces is 4. Referring to the geometry defined in Fig. 7, we can obtain the analytic solution for D_j after some algebraic manipulations as follows:

$$D_j = aL\exp[ik(\hat{e}_0-\hat{r})\cdot\mathbf{d}_i]\frac{\sin[k(\hat{e}_0-\hat{r})\cdot\mathbf{r}_4/2]}{k(\hat{e}_0-\hat{r})\cdot\mathbf{r}_4/2} \times\frac{\sin[k(\hat{e}_0-\hat{r})\cdot\mathbf{c}_i/2]}{k(\hat{e}_0-\hat{r})\cdot\mathbf{c}_i/2}, \qquad j=1,2,3, \quad \text{(A3a)}$$

$$\begin{aligned} D_4 = \frac{\sqrt{3}}{2}a^2\Bigg\{ &\exp[ik(\hat{e}_0-\hat{r})\cdot(\mathbf{r}_4+\mathbf{r}_1+\mathbf{r}_2)/2] \\ &\times\frac{\sin[k(\hat{e}_0-\hat{r})\cdot\mathbf{r}_1/2]}{k(\hat{e}_0-\hat{r})\cdot\mathbf{r}_1/2}\frac{\sin[k(\hat{e}_0-\hat{r})\cdot\mathbf{r}_2/2]}{k(\hat{e}_0-\hat{r})\cdot\mathbf{r}_2/2} \\ &+\exp[ik(\hat{e}_0-\hat{r})\cdot(\mathbf{r}_4+\mathbf{r}_2+\mathbf{r}_3)/2] \\ &\times\frac{\sin[k(\hat{e}_0-\hat{r})\cdot\mathbf{r}_2/2]}{k(\hat{e}_0-\hat{r})\cdot\mathbf{r}_2/2}\frac{\sin[k(\hat{e}_0-\hat{r})\cdot\mathbf{r}_3/2]}{k(\hat{e}_0-\hat{r})\cdot\mathbf{r}_3/2} \\ &+\exp[ik(\hat{e}_0-\hat{r})\cdot(\mathbf{r}_4+\mathbf{r}_3+\mathbf{r}_1)/2] \\ &\times\frac{\sin[k(\hat{e}_0-\hat{r})\cdot\mathbf{r}_3/2]}{k(\hat{e}_0-\hat{r})\cdot\mathbf{r}_3/2}\frac{\sin[k(\hat{e}_0-\hat{r})\cdot\mathbf{r}_1/2]}{k(\hat{e}_0-\hat{r})\cdot\mathbf{r}_1/2}\Bigg\}, \end{aligned} \quad \text{(A3b)}$$

where a and L are the semiwidth and the length of a hexagonal ice crystal, respectively. The vectors $\mathbf{r}_j$ ($j=1,\ldots,4$), $\mathbf{d}_j$ ($j=1,2,3$), and $\mathbf{c}_j$ ($j=1,2,3$) are defined in Fig. 7.

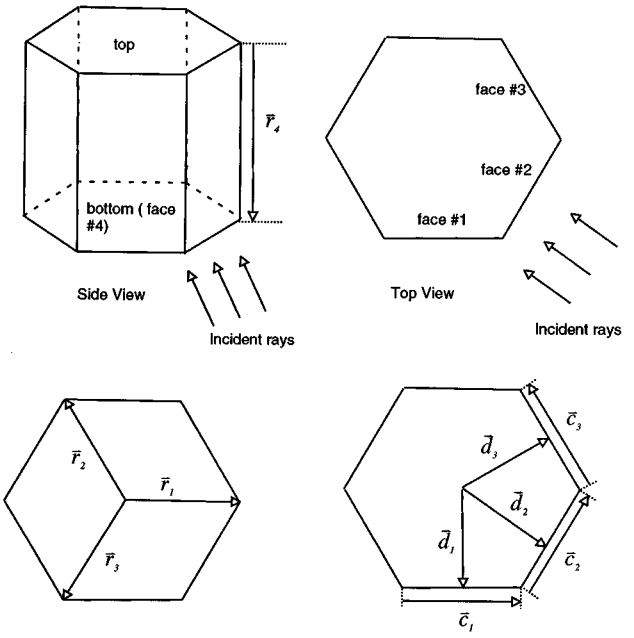

Fig. 7. Geometry of the incident rays with respect to a hexagonal ice crystal.

ACKNOWLEDGMENTS

This study was supported by National Science Foundation (NSF) grant ATM-93-1521 and in part by NASA grants NAG1-1719 and NAG5-2678 and U.S. Department of Energy grant DE-FG03-95ER 61991. The FDTD results presented in this paper were obtained from the use of CRAY Y-MP 8/864 at the National Center for Atmospheric Research, which is sponsored by the NSF. The authors thank the anonymous reviewer for constructive comments and suggestions.

Address correspondence to Ping Yang at the location on the title page or tel: 801-585-9480; fax: 801-581-4065; e-mail: yang@climate.met.utah.edu

REFERENCES

1. K. N. Liou, "Influence of cirrus clouds on weather and climate process: a global perspective," Mon. Weather Rev. **114**, 1167–1199 (1986).
2. G. L. Stephens, S. C. Tsay, P. W. Stackhouse, and P. J. Flatau, "The relevance of the microphysical and radiative properties of cirrus clouds to climate and climate feedback," J. Atmos. Sci. **46**, 1742–1753 (1990).
3. K. N. Liou and Y. Takano, "Light scattering by nonspherical particles: remote sensing and climate implications," Atmos. Res. **31**, 271–298 (1994).
4. A. Ono, "The shape and riming properties of ice crystals in natural clouds," J. Atmos. Sci. **26**, 138–147 (1969).
5. A. J. Heymsfield, "Laboratory and field observations of the

growth of columnar and plate crystals from frozen droplets," J. Atmos. Sci. **30**, 1650–1656 (1973).
6. A. J. Heymsfield, "Cirrus uncinus generating cells and the evolution of cirrusform clouds. Part I: Aircraft observations of the growth of the ice phase," J. Atmos. Sci. **32**, 799–808 (1975).
7. A. J. Heymsfield, K. M. Miller, and J. D. Sphinhirne, "The 27–28 October 1986 FIRE IFO cirrus case study: cloud microstructure," Mon. Weather Rev. **118**, 2313–2328 (1990).
8. K. Sassen, "Air-truth lidar polarization studies of orographic clouds," J. Appl. Meteorol. **17**, 73–91 (1978).
9. R. T. Bruintjes, A. J. Heymsfield, and T. W. Krauss, "An examination of double-plate ice crystals and initiation of precipitation in continental cumulus clouds," J. Atmos. Sci. **44**, 1331–1349 (1987).
10. S. C. Ou, K. N. Liou, W. Gooch, and Y. Takano, "Remote sensing of cirrus cloud parameters using advantaged very-high-resolution radiometer 3.7- and 10.9-μm channels," Appl. Opt. **32**, 2171–2180 (1993).
11. S. Kinne and K. N. Liou, "The effects of the nonsphericity and size distribution of ice crystals on the radiative properties of cirrus clouds," Atmos. Res. **24**, 273–284 (1989).
12. P. Yang and K. N. Liou, "Light scattering by hexagonal ice crystals: comparison of finite-difference time domain and geometric optics models," J. Opt. Soc. Am. A **12**, 162–176 (1995).
13. Q. Cai and K. N. Liou, "Polarized light scattering by hexagonal ice crystals: theory," Appl. Opt. **21**, 3569–3580 (1982).
14. Y. Takano and K. N. Liou, "Solar radiative transfer in cirrus clouds. Part I: Single-scattering and optical properties of hexagonal ice crystals," J. Atmos. Sci. **46**, 1–19 (1989).
15. A. Macke, "Scattering of light by polyhedral ice crystals," Appl. Opt. **32**, 2780–2788 (1993).
16. H. C. van de Hulst, *Light Scattering by Small Particles* (Wiley, New York, 1957).
17. D. S. Saxon, "Lectures on the scattering of light," in *Proceedings of the UCLA International Conference on Radiation and Remote Probing of the Atmosphere*, J. G. Kuriyan, ed. (Western Periodicals, North Hollywood, Calif., 1973), pp. 227–308.
18. J. D. Jackson, *Classic Electrodynamics*, 2nd ed. (Wiley, New York, 1975).
19. G. H. Goedecks and S. G. O'Brien, "Scattering by irregular particles via the digitized Green's function algorithm," Appl. Opt. **27**, 2431–2438 (1981).
20. E. M. Purcell and C. P. Pennypacker, "Scattering and absorption of light by nonspherical dielectric grains," Astrophys. J. **196**, 705–714 (1973).
21. P. Yang and K. N. Liou, "Finite-difference time domain method for light scattering by small ice crystals in three-dimensional space," J. Opt. Soc. Am. A **13**, 2072–2085 (1996).
22. C. Acquista, "Light scattering by tenuous particles: a generalization of the Rayleigh–Gans–Rocad approach," Appl. Opt. **15**, 2932–2936 (1976).
23. K. S. Shifrin, "Scattering of light in a turbid medium," NASA Tech. Transl. TTF-477 (National Technical Information Service, Springfield, Va., 1968).
24. J. D. Klett and A. Sutherland, "Approximate methods for modeling the scattering properties of nonspherical particles: evaluation of the Wentzel–Kramers–Brillouin method," Appl. Opt. **31**, 373–386 (1992).
25. T. W. Chen, "High energy light scattering in the generalized eikonal approximation," Appl. Opt. **28**, 4096–4102 (1989).
26. G. L. Stephens, "Scattering of plane wave by soft obstacles: anomalous diffraction theory for circular cylinders," Appl. Opt. **23**, 954–959 (1984).
27. P. Chylek and J. D. Klett, "Absorption and scattering of electromagnetic radiation by prismatic columns: anomalous diffraction approximation," J. Opt. Soc. Am. A **8**, 1713–1720 (1991).
28. P. Yang and K. N. Liou, "Geometric-optics-integral-equation method for light scattering by nonspherical ice crystals," Appl. Opt. **53**, 6568–6584 (1996).
29. S. A. Schekunoff, *Electromagnetic Waves* (Van Nostrand, New York, 1943).